Surface & Coatings Technology 496 (2025) 131644

Contents lists available at ScienceDirect

Surface & Coatings Technology

journal homepage: www.elsevier.com/locate/surfcoat

Synthesis of $Al_xCoCrFeNi$ HEA thin films by high power impulse magnetron sputtering: Effect of substrate bias voltage

Alessandro Togni [a,*], Francesco Montagner [b], Enrico Miorin [b], Cecilia Mortalò [b], Valentina Zin [b,*], Giovanni Bolelli [a], Luca Lusvarghi [a], Stefano Frabboni [c], Gian Carlo Gazzadi [d], Lidia Armelao [e,f], Silvia Maria Deambrosis [b]

[a] Department of Engineering "Enzo Ferrari", University of Modena and Reggio Emilia, Via P. Vivarelli 10, 41125 Modena, Italy
[b] Institute of Condensed Matter Chemistry and Technologies for Energy (ICMATE), National Research Council (CNR), Corso Stati Uniti 4, 35127 Padova, Italy
[c] Department of Physics, Informatics and Mathematics, University of Modena and Reggio Emilia, Via G. Campi 213/A, 41125 Modena, Italy
[d] Institute of Nanoscience (NANO), National Research Council (CNR), Via G. Campi 213/A, 41125 Modena, Italy
[e] Department of Chemical Sciences, University of Padova, Via F. Marzolo 1, 35131 Padova, Italy
[f] Department of Chemical Sciences and Materials Technology (DSCTM), National Research Council (CNR), Piazzale A. Moro 7, 00185 Roma, Italy

ARTICLE INFO

Keywords:
High entropy alloys
High power impulse magnetron sputtering
Bias voltage
Microstructure
Mechanical properties
Tribocorrosion

ABSTRACT

In this study, $Al_xCoCrFeNi$ high entropy alloy (HEA) thin films were deposited by high power impulse magnetron sputtering (HiPIMS) to explore the effect of substrate bias voltage on their microstructure, mechanical properties, and corrosion and tribocorrosion behavior. Si (100) and AISI 304 stainless steel (SS) were used as substrates, with the latter also serving as a reference for comparative purposes. Higher bias voltages promoted the formation of a dense, fine-grained microstructure, which positively affected the electrochemical performance of the films in a 3.5 wt.% NaCl aqueous solution. When the bias voltage exceeded −70 V, the Al content decreased from 10 to 5 at.%. As a result, the crystal structure transitioned from a dual-phase face-centered cubic (FCC) + body-centered cubic (BCC) structure to a single-phase FCC structure. While the residual stress state within the films shifted from tensile to compressive with increasing bias voltage, their hardness remained relatively constant at ~9 GPa. However, some differences were found in terms of tribocorrosion behavior, with the wear rate exhibiting a non-linear trend with increasing bias voltage. Optimal wear performance was achieved at intermediate bias voltages, while excessive bias voltage values resulted in increased material loss. Nevertheless, all films demonstrated superior corrosion and tribocorrosion resistance compared to the AISI 304 SS substrate. These findings underscore the importance of adjusting the substrate bias voltage in the deposition of HEA thin films via HiPIMS to optimize their performance in wear- and corrosion-prone applications.

1. Introduction

High entropy alloys (HEAs), distinguished by their unique composition consisting of multiple elements in near-equiatomic proportions [1], have emerged as a promising class of materials offering enhanced mechanical strength [2], excellent thermal stability [3], and superior resistance to both wear [4] and corrosion [5]. These properties make HEAs suitable candidates for use as thin films and coatings, where they have the potential to outperform traditional materials in harsh environments [6].

Over the years, several deposition techniques have been employed to produce HEA thin films and coatings, including magnetron sputtering [7–9], thermal spraying [10–12], electrochemical deposition [13,14], and laser cladding [15,16]. Among these methods, magnetron sputtering has proven particularly promising for synthesizing HEA thin films, primarily because of its ability to precisely control the film stoichiometry by adjusting both the chemical composition of the target material and the process parameters during deposition [6].

In conventional direct current magnetron sputtering (DCMS), plasma densities typically range from 10^{15} to 10^{17} m^{-3} [17], resulting in relatively low ionization probabilities of the sputtered atoms. As a result, the metal ion-to-neutral ratio in the deposition flux is generally only a few percent [18,19], which can lead to the formation of less compact and potentially defective films. To overcome this limitation, in 1999,

* Corresponding authors.
E-mail addresses: alessandro.togni@unimore.it (A. Togni), valentina.zin@cnr.it (V. Zin).

https://doi.org/10.1016/j.surfcoat.2024.131644
Received 24 July 2024; Received in revised form 27 November 2024; Accepted 6 December 2024
Available online 9 December 2024

Kouznetsov et al. [20] introduced a novel pulsed magnetron sputter deposition technique, later named high power impulse magnetron sputtering (HiPIMS).

In HiPIMS, high-power pulses are applied to the target at low duty cycles and repetition frequencies, achieving peak target power densities of several kW/cm^2 while maintaining average target power densities at levels that prevent overheating and subsequent melting of the target material [21,22]. This unique mode of operation generates a highly dense plasma with peak electron densities exceeding 10^{19} m^{-3} near the target [23,24]. Consequently, electron-impact ionization of the sputtered atoms is significantly enhanced, resulting in ionization levels as high as 90 % [25]. Films deposited via HiPIMS typically exhibit denser microstructures and smoother surfaces than those produced by DCMS [26,27]. In addition, the high degree of ionization allows precise control of the kinetic energy of the bombarding ion flux during film growth, e.g., by applying a negative bias voltage to the substrate [21,22].

However, there are only a few studies on the influence of substrate bias voltage on the structure and properties of HEA thin films deposited by HiPIMS [28,29]. For instance, Xu et al. [28] investigated the effect of bias voltage on the microstructure and mechanical properties of (AlCrTiVZr)N films synthesized by HiPIMS. Their findings revealed a transformation of the cross-sectional morphology from a loose columnar microstructure to a dense, featureless one as the bias voltage increased from 0 to −150 V, accompanied by an increase in hardness from 25 to 48.3 GPa. However, a further increase in bias voltage to −200 V caused excessive ion bombardment, adversely affecting the mechanical properties of the films. Similar results were observed for CuNiTiNbCr films, also deposited via HiPIMS at bias voltages ranging from 0 to −200 V [29]. The film deposited at −150 V demonstrated the highest hardness value of 11.6 GPa owing to its compact, defect-free structure and compressive stress state. However, higher bias voltages led to an increase in defect concentration and a shift in stress from compressive to tensile, consequently reducing the hardness of the film.

In light of these considerations, this study explores the effect of substrate bias voltage on the microstructure, mechanical properties, and corrosion and tribocorrosion behavior of Al$_x$CoCrFeNi HEA thin films synthesized by HiPIMS. The rationale for choosing this alloy system stems from its exceptional combination of mechanical properties and corrosion resistance [30–32]. Moreover, the volume fractions of the face-centered cubic (FCC) and body-centered cubic (BCC) phases within the alloy vary with the Al concentration, allowing the properties of the alloy to be manipulated to meet specific application requirements. Specifically, increasing the Al content promotes the transition from an FCC to a BCC phase [30,31]. In this work, we chose a nominal Al concentration of 10 at.% to achieve a dual-phase structure comprising both FCC and BCC phases, thus combining the excellent toughness associated with the FCC phase with the high strength characteristic of the BCC phase [33].

2. Experimental details

2.1. Film deposition

The films were deposited by HiPIMS using pure Al and equiatomic CoCrFeNi alloy targets supplied by Shenzhen Rearth Technology Co., Ltd. Both targets, measuring ⌀ 10 cm × h 0.3 cm, were manufactured by vacuum arc melting. A detailed description of the deposition setup is available in our previous publication [34]. One-side polished Si (100) wafers and AISI 304 stainless steel (SS) plates were used as substrates. The SS plates were ground using SiC papers up to 2500 mesh and polished with a 3 μm polycrystalline diamond suspension. Before being placed into the process chamber, the substrates were cleaned with acetone and isopropanol in an ultrasonic bath for 10 min and then blow-dried with pure N_2 gas. Once cleaned, the substrates were mounted on a holder rotating at 10 rpm to ensure uniform film composition and thickness. The targets were tilted at 45° relative to the substrate surface normal, with the Al target positioned at 140 mm from the substrate surface and the CoCrFeNi target at 120 mm.

Table 1
HiPIMS deposition parameters of Al$_x$CoCrFeNi HEA thin films.

Parameter	Value
	Al / CoCrFeNi
Target-to-substrate distance (mm)	140 / 120
Ar flow rate (sccm)	175
Working pressure (Pa)	0.5
Target power (W)	100 / 500
Target pulse frequency (Hz)	250 / 250
Target pulse length (μs)	75 / 100
Substrate bias voltage (V)	0, −35, −70, −105, −140

Before deposition, the process chamber was pumped down to a background pressure of 10^{-5} Pa to minimize residual oxygen levels. Pure Ar gas was then introduced at a constant flow rate of 175 sccm, establishing a working pressure of 0.5 Pa. In addition, a preliminary 3-min pre-sputtering of the targets with the shutters closed was performed before each deposition cycle to stabilize the deposition conditions and remove surface contaminants. Subsequently, the films were deposited using the parameters outlined in Table 1. These parameters were chosen based on preliminary tests that indicated they would produce films with approximately 10 at.% of Al. The discharge voltage and current waveforms were recorded during the deposition process using a PicoScope 2406B oscilloscope (Pico Technology, St Neots, UK). The substrate bias voltage was systematically varied from 0 to −140 V in steps of 35 V while maintaining a pulse frequency of 250 Hz and a pulse length of 200 μs. Accordingly, the films were named BV0, BV35, BV70, BV105, and BV140, corresponding to their respective bias voltage values. The bias power supply was synchronized with the HiPIMS pulses with virtually zero delay to maximize ion acceleration toward the substrate, thus promoting the formation of dense films. While selectively attracting the metal ion-rich portion and minimizing the incorporation of gas ions into the growing films could further optimize film quality, as discussed in [35], this approach is beyond the scope of the present study. No external heating was applied to the substrate. However, during the deposition process, the substrate temperature increased to approximately 60 °C, as measured by thermocouples. Depending on the applied bias voltage, the deposition time was varied from 90 to 120 min to achieve a comparable film thickness of approximately 2.5 μm.

2.2. Film characterization

2.2.1. Morphology, chemical composition, microstructure, and residual stress state

The surface and cross-sectional morphology of the films deposited on Si substrates was observed using a ZEISS Sigma field emission scanning electron microscope (FE-SEM, Carl Zeiss, Oberkochen, Germany) operated at an acceleration voltage of 15 kV. Cross-sections were prepared by manually fracturing the coated Si samples. The chemical composition of the films was determined by energy dispersive X-ray spectroscopy (EDS) using an Oxford X-Max silicon drift detector (SDD, Oxford Instruments, Abingdon, UK) interfaced with the FE-SEM.

The crystal structure of the films, also deposited on Si substrates, was investigated by X-ray diffraction (XRD) using an Empyrean X-ray diffractometer (Malvern Panalytical, Malvern, UK) equipped with a Cu-Kα radiation source, operated at 40 kV and 40 mA, and a PIXcel^{3D} detector. The diffractograms were recorded in Bragg-Brentano mode over a 2θ range of 30–110° with a step size of 0.01° and a step time of 60 s. The pulse height distribution was optimized to reduce the fluorescence-induced background by setting the lower level to 64.0 % and the upper level to 80.0 %. The obtained XRD patterns were interpreted using the International Centre for Diffraction Data (ICDD) database integrated into the X'Pert HighScore Plus software from Malvern Panalytical.

Further microstructural analyses were carried out by transmission electron microscopy (TEM) and selected area electron diffraction (SAED) using a TALOS F200S G2 S/TEM (Thermo Fisher Scientific, Waltham, MA, USA) equipped with a Schottky field emitter operated at 200 kV and two SSDs for EDS analysis. The acquired data were processed using the DigitalMicrograph® software (Gatan Inc., Pleasanton, CA, USA). Electron-transparent TEM samples were prepared by focused ion beam (FIB) milling using an FEI Strata DB235M Dual Beam system, also from Thermo Fisher Scientific, operated at an acceleration voltage of 30 kV, followed by final polishing at 5 kV. Before FIB milling, a thin Pt layer was deposited on the film surface to prevent damage, redeposition artifacts, and Ga implantation during the milling process.

The in-plane residual stress of the films was estimated using the wafer curvature method. First, the curvature of the coated Si substrates was measured using a DektakXT stylus profilometer (Bruker, Billerica, MA, USA), averaging three profiles collected along two normal directions. Subsequently, the residual stress level was calculated using the modified Stoney equation [36,37].

2.2.2. Electrochemical behavior

The electrochemical behavior of the films deposited on Si substrates was evaluated by potentiodynamic polarization tests in a 3.5 wt.% NaCl aqueous solution at room temperature. The tests were carried out in a K0235 three-electrode flat cell (AMETEK Scientific Instruments, Oak Ridge, TN, USA) connected to a VersaSTAT3 potentiostat, also from AMETEK Scientific Instruments, and equipped with an Ag/AgCl/$KCl_{(sat.)}$ reference electrode and a Pt counter electrode. Before the electrochemical test, the samples were exposed to the electrolyte (with an exposed area of 1 cm^2) for 1 h to achieve a relatively stable open circuit potential (OCP), followed by a cathodic pre-polarization treatment from 0 V vs. OCP to −0.4 V vs. OCP at a scan rate of 0.5 mV/s to remove spontaneously air-formed oxides on the film surface. Potentiodynamic polarization curves were then recorded from −0.4 V vs. OCP to 1.6 V vs. OCP at a scan rate of 0.5 mV/s. After the electrochemical test, the corrosion potential (E_{corr}) and corrosion current density (i_{corr}) of the films were obtained by fitting the linear segments of the anodic and cathodic polarization curves at an overpotential of at least |50| mV, following the Tafel extrapolation method. Each experiment was repeated three times for each sample to ensure data consistency and reliability.

2.2.3. Mechanical properties and scratch behavior

The mechanical properties of the films deposited on SS substrates were assessed according to UNI EN ISO 14577-4 using a NanoTest system (Micro Materials, Wrexham, UK) equipped with a Berkovich diamond indenter. The penetration depth of the indenter was maintained below one-tenth of the film thickness to minimize the influence of the substrate on the measured mechanical properties [38]. A total of 25 indentations were performed on each sample, using a loading/unloading rate of 0.15 mN/s and a 5-s holding time at the maximum applied load. In addition, a 30-s holding time was applied after reaching 20 % of the peak load during unloading for thermal drift correction. The hardness and elastic modulus of the films were determined from the resulting load-displacement curves using the Oliver-Pharr method [39,40].

The adhesion strength between the films and the SS substrate was evaluated by scratch testing using a CETR UMT-2 tester (Bruker, Billerica, MA, USA) equipped with a Rockwell C-type diamond indenter with a 200 μm-radius tip. Three tracks were performed on each sample for reproducibility and statistical purposes. The applied load was increased linearly from 2 to 90 N over a scratch length of 8.8 mm at a sliding speed of 10 mm/min. Critical loads were identified by SEM, following the classification given in ISO 20502:2016.

2.2.4. Tribocorrosion behavior

Tribocorrosion experiments were conducted on coated SS substrates in a three-electrode cell, also coupled to a potentiostat, and mounted on a CETR UMT-2 tester (Bruker, Billerica, MA, USA) in linear reciprocating ball-on-plate configuration, as illustrated in Fig. 1. The tests were carried out in a 3.5 wt.% NaCl aqueous solution at 30 °C. Before the sliding wear test, the OCP was monitored for 30 min. The sliding wear test was then initiated with a normal load of 0.6 N, corresponding to an initial Hertzian contact pressure of 750 MPa. The stroke length, frequency, and sliding wear time were set at 2 mm, 1 Hz, and 30 min, respectively. A 5 mm-diameter Al_2O_3 ball (RGPBALLS, Milan, Italy), manufactured according to ASTM F2094/F2094M, was used as the counterpart. During the sliding wear test, the coefficient of friction (COF) and OCP values were recorded. After the sliding wear test, an additional 30-min OCP measurement was performed to restore the initial passivation conditions. Each sample was tested twice to ensure reliable results.

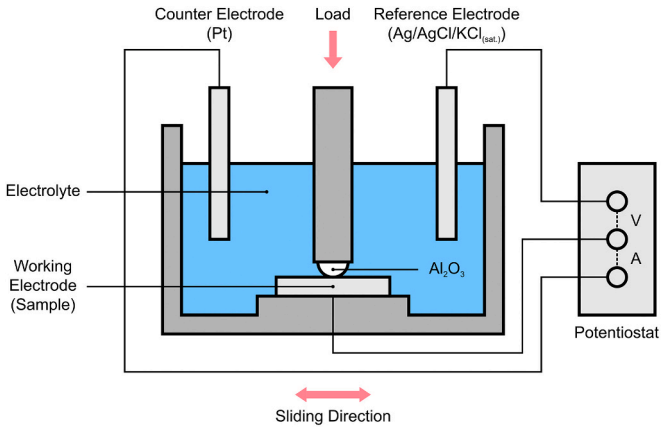

Fig. 1. Schematic representation of the tribocorrosion test setup.

Following the tribocorrosion experiments, the volume of the wear tracks was measured using a non-contact, structured light profilometer (Confovis GmbH, Jena, Germany) coupled to an ECLIPSE LV150N optical microscope (Nikon, Tokyo, Japan). The specific wear rate (k) was calculated as:

$$k = \frac{V}{N \cdot d} \tag{1}$$

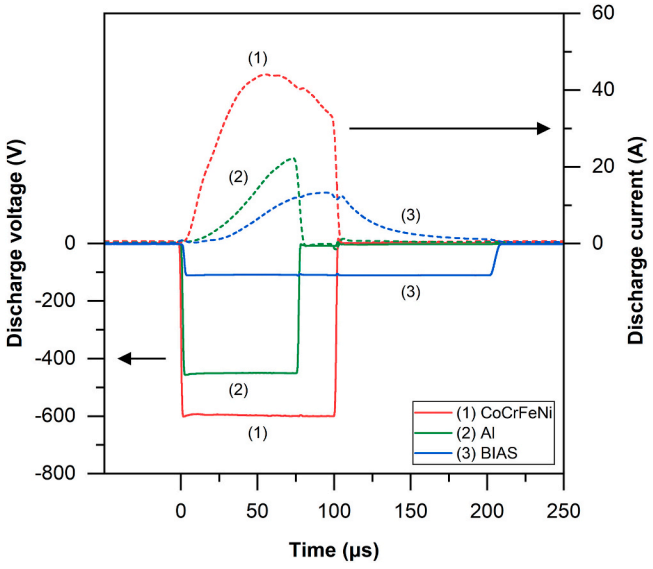

Fig. 2. Temporal evolution of the discharge voltage and current waveforms for CoCrFeNi and Al targets, recorded at a substrate bias voltage of −105 V. The solid lines correspond to the discharge voltages, and the dashed lines to the discharge currents.

Table 2
Deposition rate and chemical composition of $Al_xCoCrFeNi$ HEA thin films deposited by HiPIMS at various substrate bias voltages.

Sample	Deposition rate (nm/min)	Atomic concentration (at.%)				
		Al	Co	Cr	Fe	Ni
BV0	28	9.6 ± 0.2	23.4 ± 0.2	23.2 ± 0.1	22.1 ± 0.2	21.8 ± 0.1
BV35	29	9.4 ± 0.1	23.2 ± 0.1	23.8 ± 0.2	22.1 ± 0.1	21.5 ± 0.2
BV70	30	9.5 ± 0.1	23.0 ± 0.1	24.3 ± 0.1	22.1 ± 0.1	21.0 ± 0.1
BV105	24	6.1 ± 0.1	24.6 ± 0.2	24.5 ± 0.1	22.8 ± 0.2	22.1 ± 0.2
BV140	24	5.0 ± 0.1	25.1 ± 0.2	25.6 ± 0.1	22.7 ± 0.1	21.5 ± 0.1

where V is the wear volume, N is the normal load, and d is the total sliding distance.

The wear mechanism was investigated using a Nova NanoSEM 450 microscope (FEI - Thermo Fisher Scientific, Hillsboro, OR, USA) equipped with a field emission gun (FEG) source and a QUANTAX 200 EDS system (Bruker, Billerica, MA, USA) with an XFlash® 6–10 SSD. Three-dimensional-like morphology imaging of the worn surfaces was carried out at an acceleration voltage of 5 kV using a through-lens detector (TLD) operated in custom mode with a suction tube voltage of −10 eV. To further refine the surface details, the surface of the samples was tilted at 40° relative to the incident electron beam.

The composition of the passivation film formed within the wear track was analyzed by micro-Raman spectroscopy using a LabRAM HR Evolution confocal Raman microscope (HORIBA, Kyoto, Japan). A 532 nm-wavelength laser, focused through a 100× objective lens onto the sample surface, was used alongside a 600 grooves/mm diffraction grating. Raman spectra were acquired over a scan range of 100–1500 cm^{-1} with an acquisition time of 10 s and five accumulations. Data analysis was conducted using the LabSpec6 software from HORIBA.

3. Results and discussion

3.1. HiPIMS discharge characteristics

Fig. 2 shows the discharge voltage and current waveforms of the HiPIMS pulse for the CoCrFeNi and Al targets. Despite variations in the bias voltage, the shapes and amplitudes of the discharge voltage and current curves remain constant across the different deposition processes. Therefore, only the waveforms recorded at a bias voltage of −105 V are illustrated for reference. The CoCrFeNi and Al targets display rectangular-shaped voltage peaks, stabilizing at −600 V and −450 V, respectively. For the CoCrFeNi target, the discharge current initially rises to 45 A within the first 50–60 μs, followed by a gradual decrease, likely due to gas rarefaction. In contrast, the Al target exhibits a peak current of approximately 22 A toward the end of the pulse, around 75 μs. Regarding the substrate bias waveforms, the bias current peaks at 13 A in the 75–100 μs range before gradually decreasing over time.

3.2. Deposition rate and chemical composition

The deposition rate and chemical composition of the films deposited at various substrate bias voltages are reported in Table 2. Initially, as the bias voltage increases (in absolute value) from 0 to −70 V, the deposition rate increases from 28 to 30 nm/min. However, a further increase in bias voltage significantly reduces the deposition rate to 24 nm/min. This variation in deposition rate can be attributed to an increase in the energy of the bombarding ion flux (U_k), which is positively correlated with the bias voltage, as described by the following Equation:

$$U_k \propto \frac{D_w V_s}{P_g^{0.5}} \quad (2)$$

where D_w is the target power, V_s is the substrate bias voltage, and P_g is the working pressure [41]. Since the target power and working pressure remain constant during the deposition process, the kinetic energy of the ions bombarding the growing film increases as the bias voltage increases. However, excessive ion energy can induce re-sputtering effects, causing atoms to be ejected from the film rather than contributing to its growth. Furthermore, high-energy ions striking the film surface can enhance adatom mobility. While this can contribute to film densification by promoting the migration of atoms toward vacancies within the film, it can also lead to an overall decrease in the deposition rate [42,43].

As indicated in Table 2, the atomic concentrations of Co, Cr, Fe, and Ni within the films slightly deviate from the nominal target composition, likely due to differences in their sputtering and re-sputtering yields [44]. When the bias voltage exceeds −70 V, the Al content decreases, accompanied by a slight increase in the atomic concentrations of the other elements. This reduction in Al content can be attributed to its lower atomic weight compared to the other alloying elements, which causes its preferential re-sputtering from the films by high-energy incident ions [28,45].

3.3. Morphology and microstructure

Fig. 3 shows the surface and cross-sectional SEM micrographs of the films deposited under different substrate bias voltages. These images reveal a microstructural evolution with increasing bias voltage, transitioning from a columnar-grained structure in the unbiased film to a dense and fine structure at −140 V, where the columns are no longer visible. This phenomenon, also observed in other high entropy alloy (HEA) [29,46,47] and high entropy nitride (HEN) [28,48–52] thin films, can be attributed to the more energetic film growth conditions at higher bias voltages, which promote the migration of adsorbed atoms toward the grain boundaries, thus leading to film densification [42]. This trend is consistent with the structure zone model proposed by Anders [53], which suggests a transition from a loose columnar microstructure (Zone 1) to a fine fibrous microstructure (Zone T) as the kinetic energy of the bombarding particles increases.

The XRD patterns of the films deposited at various substrate bias voltages are displayed in Fig. 4(a). All films exhibit distinct peaks at 2θ values of 43.8° and 96.2°, corresponding to the (111) and (222) planes of a face-centered cubic (FCC) phase (ICDD 00-033-0945), respectively. Moreover, at lower bias voltages, an additional phase is visible, which can be identified as a body-centered cubic (BCC) phase (ICDD 00-035-1375), as supported by the presence of BCC (110) and BCC (220) shoulder peaks at 2θ values of 43.9° and 96.5°, respectively. Fig. 4(b) provides a more detailed view of the former peak. The absence of the BCC phase at higher bias voltages can be attributed to the reduction in Al concentration beyond −70 V, as reported in Table 2. This observation is in line with the findings of Wang et al. [31], who documented an FCC-to-BCC transformation in bulk $Al_xCoCrFeNi$ alloys (where 'x' denotes the molar ratio of Al in the alloy) with increasing Al content. Specifically, a single FCC phase was observed for $x \leq 0.4$, while the coexistence of FCC and BCC phases emerged at $x = 0.5$. Similarly, Feng et al. [54] reported the formation of a single-phase FCC solid solution in $Al_xCoCrFeNi$ thin films for $x \leq 0.3$.

In their study, Guo et al. [55] proposed using the valence electron concentration (*VEC*) to predict the stability of FCC and BCC phases in HEAs. They found that FCC phases tend to form when $VEC \geq 8$, BCC phases when $VEC < 6.87$, and a combination of FCC and BCC phases

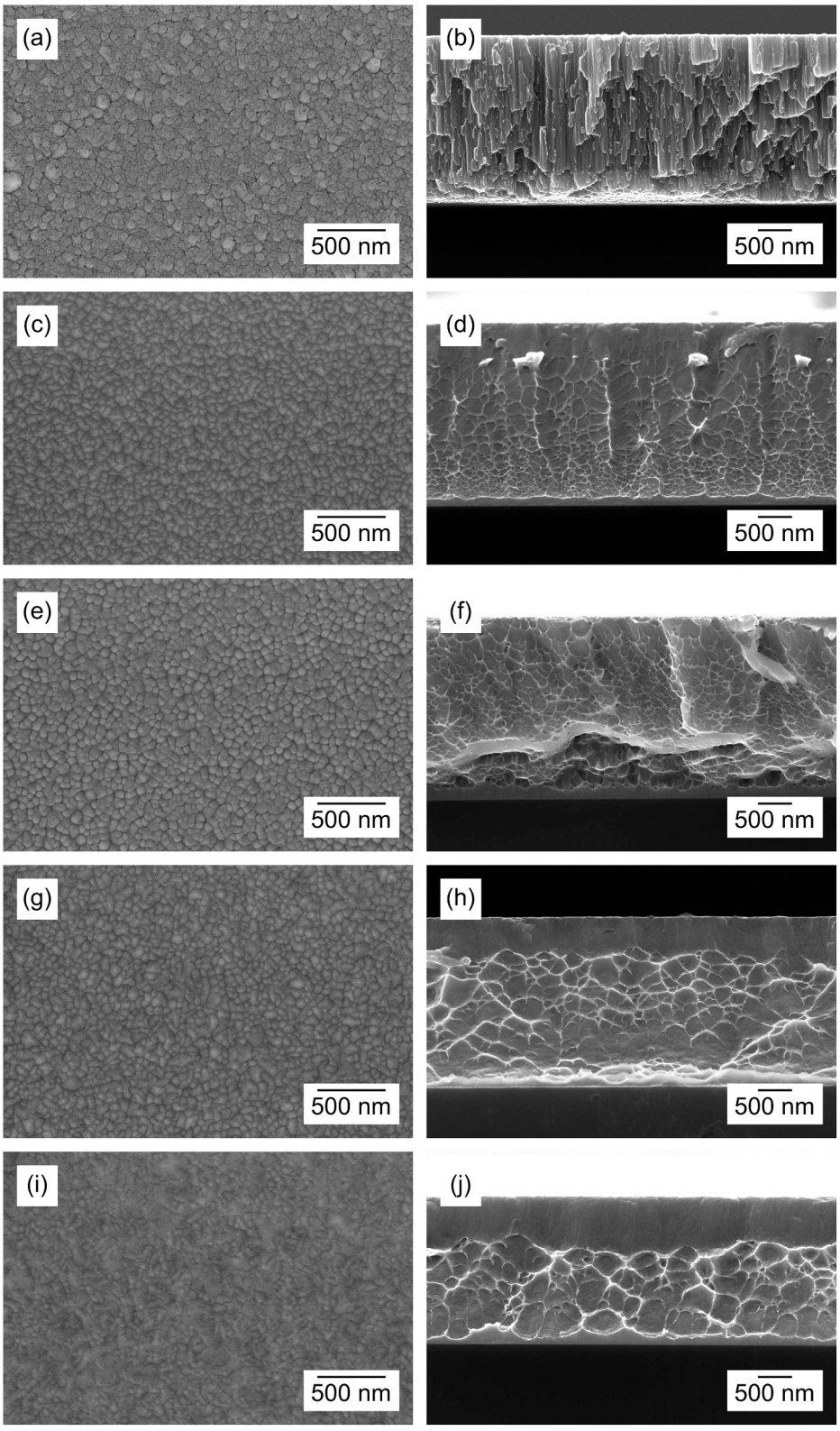

Fig. 3. SEM micrographs showing the surface (left side) and fractured cross-section (right side) of the (a, b) BV0, (c, d) BV35, (e, f) BV70, (g, h) BV105, and (i, j) BV140 films deposited on Si substrates.

when *VEC* falls between 6.87 and 8. The *VEC* is calculated as follows:

$$VEC = \sum_{i=1}^{n} c_i (VEC)_i \tag{3}$$

where n is the total number of elements, while c_i and $(VEC)_i$ are the atomic and valence electron concentrations of the i-th element, respectively. In this work, the elemental concentrations, given in Table 2, were determined by EDS, while the $(VEC)_i$ values were taken from the study conducted by Guo et al. [56]. The computed values of *VEC* for the BV0, BV35, BV70, BV105, and BV140 films are 7.73, 7.72, 7.68, 7.90, and

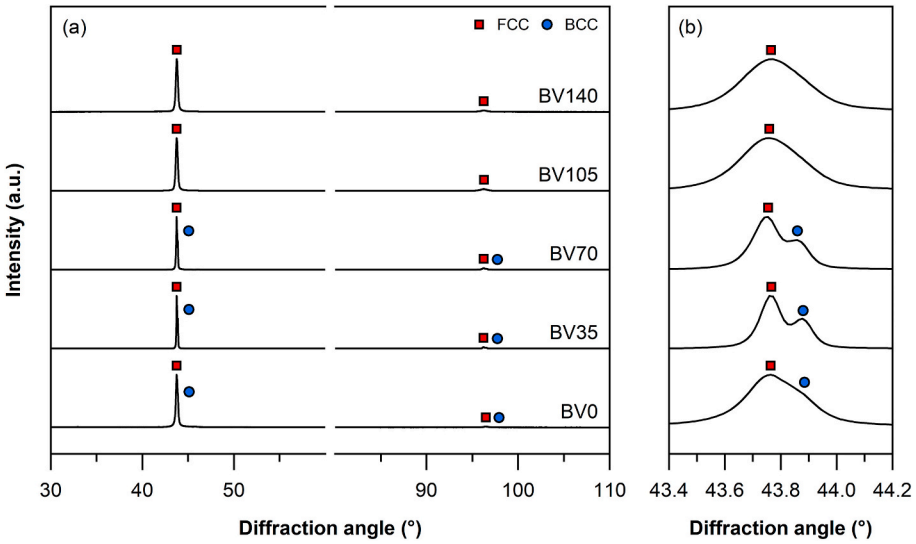

Fig. 4. (a) XRD patterns of $Al_xCoCrFeNi$ HEA thin films deposited by HiPIMS under different substrate bias voltages and (b) zoomed inset of the diffraction peaks in the 2θ range of 43.4–44.2°.

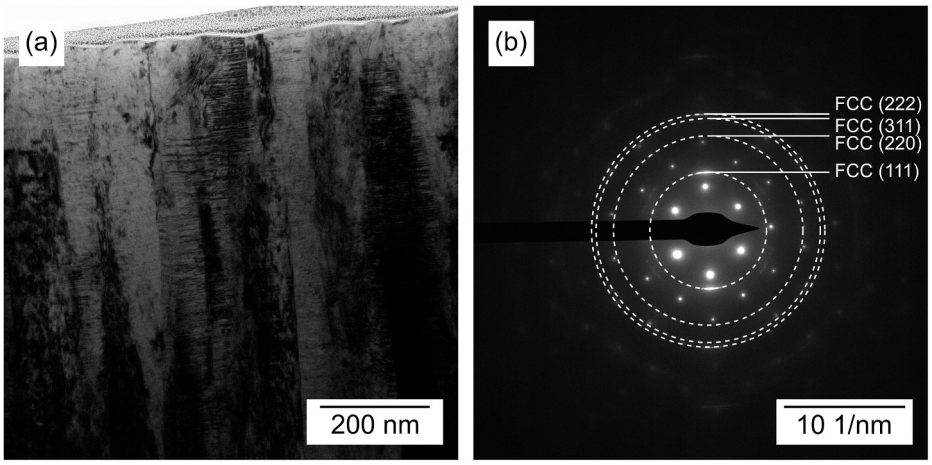

Fig. 5. (a) Cross-sectional bright-field TEM micrograph and (b) SAED pattern of the BV140 film. The bright spots in the SAED pattern correspond to single-crystal reflections from the Si substrate and serve as reference points for calibrating the interplanar distances.

7.91, respectively. These values indicate that all films meet the criteria for obtaining a dual-phase structure [55], as opposed to the XRD results (Fig. 4).

To further investigate the structure of the films deposited at higher bias voltages, the BV140 sample was analyzed by TEM. As shown in Fig. 5(a), the film exhibits a columnar growth morphology, with columnar grains measuring approximately 50 nm in width. The narrow width of these columns explains why they were not evident in the SEM micrograph of the fractured cross-section in Fig. 3(j). In addition, stacking faults and nanotwins are visible within these columns, the formation of which can be partially attributed to the low stacking fault energy (20–25 $mJ{\cdot}m^{-2}$) of these alloy systems [57]. The corresponding SAED pattern (Fig. 5(b)) reveals four distinct diffraction rings with interplanar spacings of 0.208, 0.127, 0.108, and 0.104 nm, corresponding to the (111), (220), (311), and (222) planes of an FCC phase, respectively. However, there is no evidence supporting the coexistence of a BCC phase. It is worth noting that the *VEC* values for the BV105 and BV140 films are very close to the threshold for forming the FCC phase [55]. Hence, it is plausible that the BCC phase is either undetectable or absent in these samples.

3.4. Residual stress state and mechanical properties

Fig. 6 illustrates the evolution of the residual stress within the films upon varying the substrate bias voltage. Beyond a bias voltage of −70 V, the residual stress state shifts from tensile to compressive, consistent with previous studies [49,50,58]. Residual stresses in films produced via physical vapor deposition (PVD) typically consist of thermal and intrinsic stresses. Thermal stresses arise due to differences in coefficients of thermal expansion (CTE) between the film and the substrate, while intrinsic stresses result from energetic particles bombarding the film surface [59]. In this work, no external heating was applied to the substrate during deposition, making intrinsic stress the dominant contributor to the residual stress state.

As the bias voltage increases, the energy of the ions bombarding the film surface also increases. At sufficiently high bias voltages, these energetic ions can penetrate beneath the surface of the growing film rather than depositing on it. This phenomenon, known as subplantation, leads to local densification within the film, which induces the buildup of compressive residual stresses as the implanted ions occupy the interstitial sites and compact the atomic structure [60]. Concurrently, high-energy ion bombardment can generate lattice defects, such as Frenkel

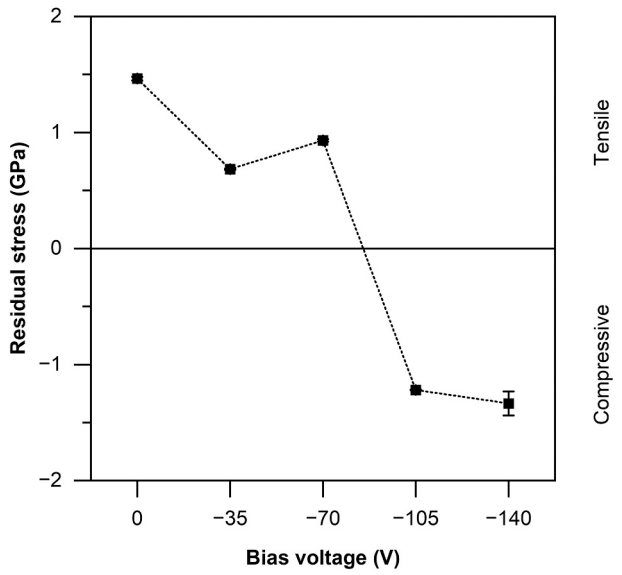

Fig. 6. Evolution of residual stress within $Al_xCoCrFeNi$ HEA thin films as a function of substrate bias voltage.

Table 3
Mechanical properties of $Al_xCoCrFeNi$ HEA thin films deposited by HiPIMS at various substrate bias voltages.

Sample	H_{IT} (GPa)	E_{IT} (GPa)
BV0	8.8 ± 0.3	254 ± 14
BV35	8.9 ± 0.3	265 ± 12
BV70	9.0 ± 0.3	259 ± 16
BV105	8.9 ± 0.3	264 ± 12
BV140	9.2 ± 0.3	244 ± 9

pairs and anti-Schottky defects, which contribute to lattice distortion and further affect the residual stress state [59,61,62].

Furthermore, as indicated in Table 2, higher bias voltages reduce the Al content in the films, as Al atoms, being lighter, are more easily re-sputtered [28,45]. This variation in composition promotes a structural transition from a mixed FCC + BCC structure to a single-phase FCC structure, as supported by the XRD and SAED analyses in Section 3.3. The volume changes accompanying this phase transformation, if significant, can introduce additional stresses. However, further investigation is needed to quantify the relative contributions of the applied bias voltage and the Al-driven phase transformation to the overall residual stress state.

The values of indentation hardness (H_{IT}) and elastic modulus (E_{IT}) of the films deposited under different substrate bias voltages are presented in Table 3. The results indicate that both hardness and elastic modulus show minimal variations with the bias voltage, averaging around 9 GPa and 260 GPa, respectively. Several factors, including microstructure and residual stress state, generally influence film hardness. As evidenced by the SEM micrographs in Section 3.3, the more energetic film growth conditions associated with higher bias voltages promote the formation of a dense, fine-grained structure, significantly reducing voids within the films and thus producing a boundary-strengthening effect [28,63]. Additionally, compressive residual stresses, as reported in other studies [28,50,51,64], can affect film hardness, as they arise from the generation of defects that can restrict plastic flow during deformation [65]. Here, while the residual stress state shifts from tensile to compressive with the applied bias voltage, the film hardness remains constant. Similar results were reported by Wang et al. [58], who manipulated the residual stress in sputtered CoCrFeNi thin films from tensile to compressive by adjusting the substrate bias voltage without significantly altering the film hardness. In our study, the observed constancy in hardness can be attributed to the interplay of competing strengthening mechanisms. At lower bias voltages, the films exhibit a higher concentration of Al and a dual-phase FCC + BCC structure. First, the incorporation of Al, with its relatively large atomic radius, induces local lattice distortion within the CoCrFeNi matrix, which, to some extent, hinders the movement of dislocations and thus increases hardness [66]. Second, the BCC phase contributes to film hardness by offering higher resistance to deformation due to its fewer slip systems compared to the FCC phase [33]. Moreover, the higher density of phase boundaries within this dual-phase structure creates additional obstacles to dislocation motion, further strengthening the films [31]. At higher bias voltages, while the increased density and compressive residual stresses would typically increase film hardness, these effects are counterbalanced by the simultaneous reduction in Al content and the transition to a single-phase FCC structure, resulting in a near-constant hardness.

3.5. Scratch behavior

Fig. 7 shows the magnified views of the scratch tracks of the films deposited at various substrate bias voltages. For the unbiased sample, semi-circular, finely spaced cracks are visible at the very beginning of the scratch track (Fig. 7(a)), indicating a lower critical load (L_{c1}) of 2 N. These cracks likely result from tensile stresses generated at the rear side of the indenter [67,68], superimposed on the pre-existing tensile residual stress state within the film. In fact, the residual stress values in Fig. 6 presumably also apply to the films deposited on the stainless steel substrate. As discussed in Section 3.4, the measured residual stresses in the films are due to intrinsic stresses related to the process conditions rather than thermal stresses, which are instead influenced by the CTE of the substrate material. At an applied load of approximately 38 N, brittle delamination of the film occurs on the trackside (Fig. 7(b)), possibly due to stresses induced by the bending of the stiffer film onto the softer substrate. As the bias voltage increases (in absolute value) from 0 to −35 V and −70 V, initial surface breakage within the scratch track occurs at approximately 9 N (Fig. 7(c, e)). With a further increase in bias voltage, no obvious tensile cracks are visible within the scratch track (Fig. 7(g, i)), making the measurement of L_{c1} values unfeasible. As the applied load increases, the number of cracks decreases, accompanied by the formation of ductile ripples along the rim of the scratch groove (Fig. 7(d, f)), indicative of a transition from predominantly brittle failure to plastic deformation. Moreover, under the experimental testing conditions of this study, there is no evidence of substrate exposure (meaning no measurable L_{c2} values), which suggests improved film-to-substrate adhesion with increasing bias voltage. The magnified views of the trackside reveal that the wrinkle-like ripples induced by plastic deformation are also visible in the films deposited at higher bias voltages (Fig. 7(h, j)). The increase in scratch toughness with increasing bias voltage can be attributed initially to a reduction in the driving force for crack propagation, as the magnitude of tensile residual stresses decreases, and subsequently to the inhibition of crack expansion due to the generation of compressive residual stresses in the films deposited at higher bias voltages, as demonstrated in Fig. 6. In addition, at higher bias voltage values, the film structure transitions from a dual-phase FCC + BCC structure to a single-phase FCC structure. This phase transition likely further enhances scratch toughness, as the FCC phase inherently offers greater ductility compared to the BCC phase [33].

3.6. Electrochemical behavior

The potentiodynamic polarization curves of the films in a 3.5 wt.% NaCl aqueous solution, together with that of AISI 304 SS, are displayed in Fig. 8. It should be mentioned that, for the corrosion tests only, the films were deposited on larger Si substrates than those used for the other measurements. However, the BV0 film deposited on these larger substrates exhibited extensive cracking and delamination after deposition,

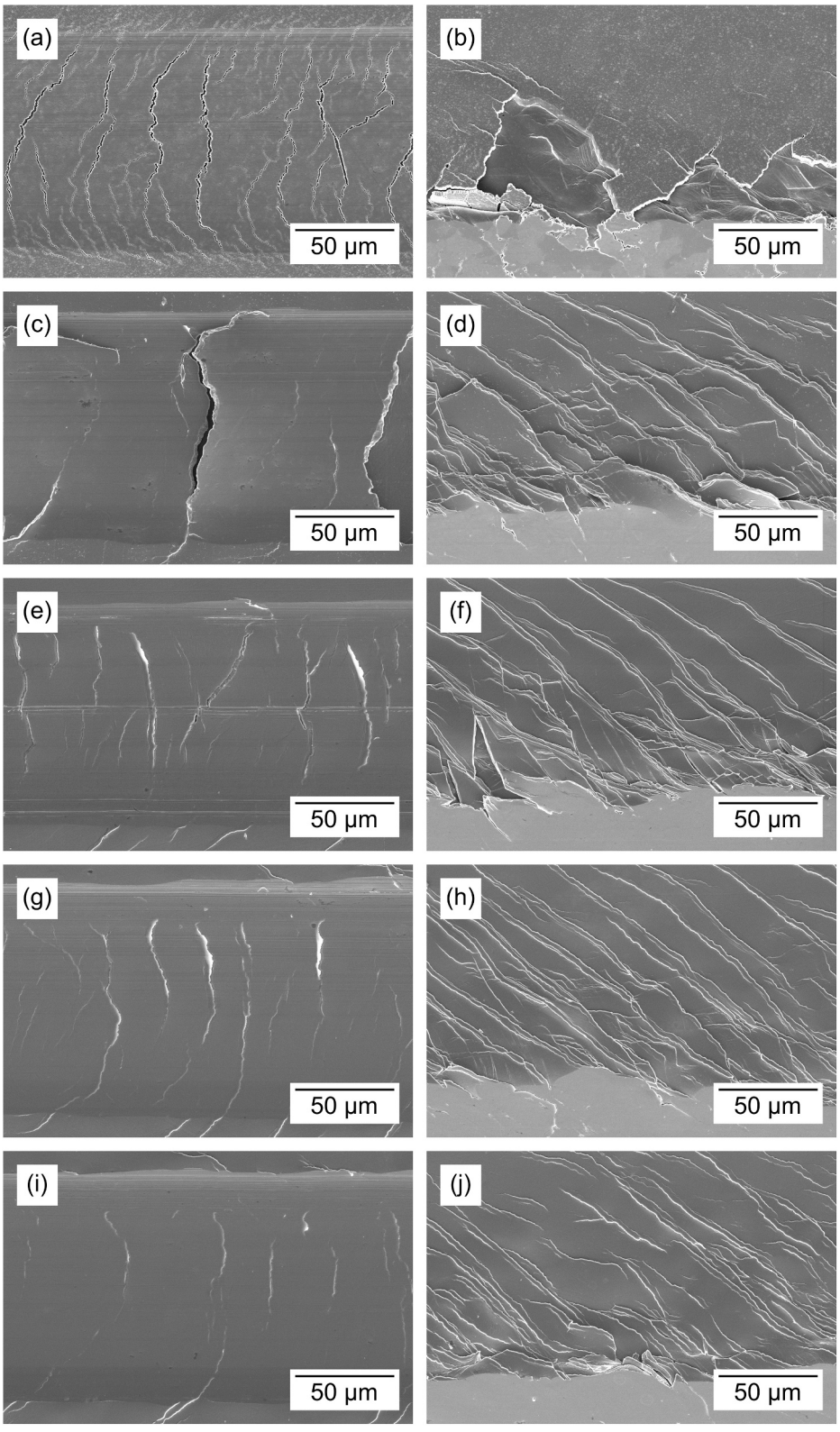

Fig. 7. SEM micrographs showing the initial segment (left side) and edge (right side) of the scratch tracks of the (a, b) BV0, (c, d) BV35, (e, f) BV70, (g, h) BV105, and (i, j) BV140 films deposited on stainless steel.

likely due to high residual stress levels, thus making corrosion testing infeasible.

The anodic segment of the polarization curves of all samples reveals an initial phase of active dissolution, followed by a passivation region associated with the formation of a protective film on the sample surface. Within this region, there is a gradual increase in potential with minimal current fluctuations.

The measured corrosion potential (E_{corr}) and corrosion current density (i_{corr}) values are listed in Table 4. Compared to stainless steel, the films demonstrate higher corrosion potentials and lower corrosion

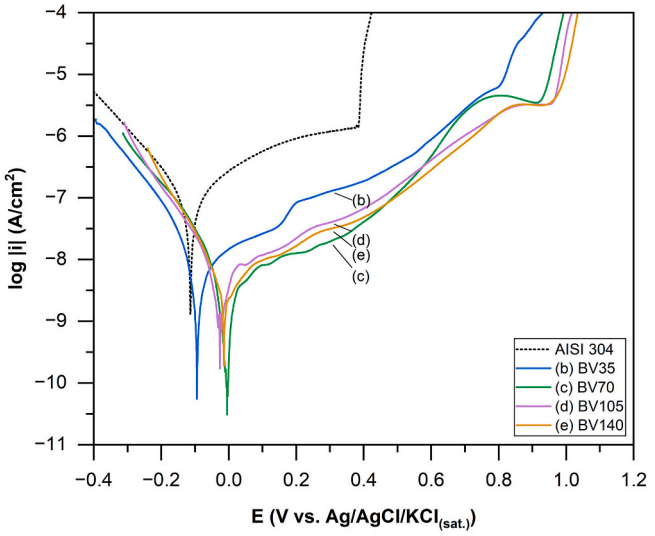

Fig. 8. Potentiodynamic polarization curves of $Al_xCoCrFeNi$ HEA thin films and AISI 304 stainless steel in a 3.5 wt.% NaCl aqueous solution.

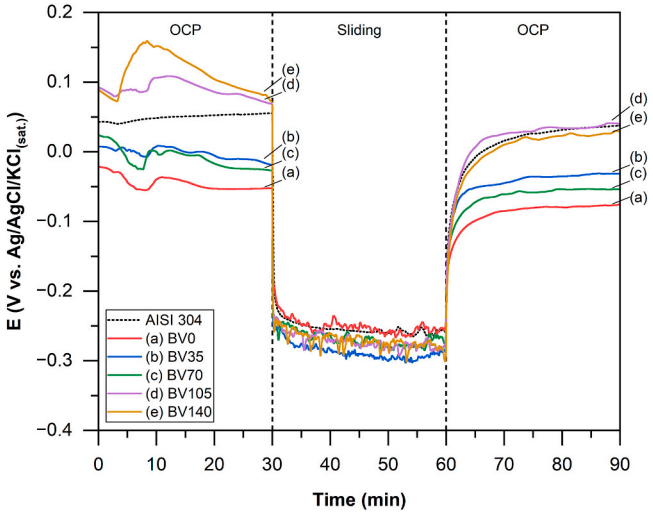

Fig. 9. OCP evolution over time for $Al_xCoCrFeNi$ HEA thin films and AISI 304 stainless steel during tribocorrosion testing in a 3.5 wt.% NaCl aqueous solution.

Table 4
Electrochemical parameters of $Al_xCoCrFeNi$ HEA thin films and AISI 304 stainless steel obtained from the potentiodynamic polarization curves in Fig. 8 using the Tafel extrapolation method.

Sample	E_{corr} (mV)	i_{corr} (μA/cm^2)
AISI 304	−117.4 ± 0.3	(1.1 ± 0.1) × 10^{-1}
BV35	−87 ± 10	(8.2 ± 0.1) × 10^{-3}
BV70	−6 ± 4	(4.2 ± 0.4) × 10^{-3}
BV105	0 ± 19	(6.2 ± 0.3) × 10^{-3}
BV140	−21 ± 17	(4.6 ± 0.1) × 10^{-3}

current densities, indicating superior corrosion resistance. This improved electrochemical behavior can be attributed to the higher concentration and uniform distribution of passivating elements in the films, particularly Cr, which promote the formation of a protective layer on the surface, effectively preventing chloride ions from penetrating toward the film-substrate interface [69,70]. Accordingly, the films show a significantly broader passivation range than stainless steel. Passivity breakdown occurs at approximately +1 V vs. Ag/AgCl/KCl$_{(sat.)}$ in the films, whereas transpassivation of the uncoated substrate occurs as early as +0.4 V.

Furthermore, the corrosion resistance of the films surpasses that of their corresponding bulk counterparts reported in the literature (with i_{corr} values ranging from 10^{-1} to 10^{-2} μA/cm^2 [32]). This enhancement can be attributed to the significantly higher cooling rates inherent in sputter deposition processes compared to conventional fabrication methods, which effectively limit element segregation during film growth [71]. As a result, a more uniform elemental distribution can be achieved in HEA thin films, which in turn improves their corrosion resistance [72]. Similar results were reported by Li et al. [73], who conducted a comparative study on the corrosion behavior of electrospark-deposited AlCoCrFeNi coatings and their cast equivalent. Unlike the cast material, the coatings showed no Cr-rich interdendritic segregation or nano-sized precipitates, resulting in reduced corrosion current density.

When comparing the different films, the most significant change occurs as the bias voltage increases (in absolute value) from −35 to −70 V. Within this range, the corrosion potential increases from −87 ± 10 to −6 ± 4 mV vs. Ag/AgCl/KCl$_{(sat.)}$, and the corrosion current density decreases correspondingly (Table 4). This trend is also qualitatively evident in the polarization curves in Fig. 8, where increasing the bias voltage from −35 to −70 V shifts them toward higher potentials and lower currents. However, beyond a bias voltage of −70 V, there is no discernible effect on the electrochemical behavior of the films, especially considering the experimental errors associated with the measured E_{corr} and i_{corr} values. These findings are consistent with previous studies [29,47], which attributed the enhanced corrosion resistance of the films to film densification induced by bias application. Our work reveals that the films deposited at lower bias voltages display a columnar microstructure, in which the column boundaries serve as preferential pathways for corrosive agents. In contrast, the films deposited at higher bias voltages exhibit a denser microstructure with smaller channels, which can delay the corrosive media from reaching the film-substrate interface.

In addition to microstructural refinement, the transition from a dual-phase FCC + BCC structure to a single-phase FCC structure with increasing bias voltage can also influence corrosion resistance [72]. In bulk HEAs, the formation of multiple phases often leads to the segregation of elements, which can compromise corrosion resistance by forming localized galvanic cells. However, in the thin-film form, the rapid cooling rates during deposition mitigate this effect by promoting a more homogeneous elemental distribution [71]. As a result, in regions where FCC and BCC phases coexist, the variation in chemical composition is minimal and does not substantially affect the electrochemical performance of the films, as demonstrated in [72]. Therefore, the enhanced corrosion resistance observed at higher bias voltages can be primarily attributed to the denser microstructure. Notably, the most significant improvement occurred when the bias voltage increased (in absolute value) from −35 to −70 V, correlating with microstructural refinement. In contrast, the disappearance of the detectable BCC phase at even higher bias voltages did not produce a correspondingly measurable effect on corrosion resistance.

3.7. Tribocorrosion behavior

Fig. 9 shows the temporal evolution of the open circuit potential (OCP) of the films, along with that of the AISI 304 SS substrate, recorded before, during, and after the sliding wear test in simulated seawater. Under non-contact conditions, the films deposited at lower bias voltages display lower OCP values than those deposited at higher bias voltages, possibly attributable to their loose columnar microstructure, consistent with the results of the potentiodynamic polarization tests. The electrode potential evolution follows the typical trend of metals exhibiting a passive behavior. When the sliding phase begins, the potential of all samples drops to approximately −0.25 V vs. Ag/AgCl/KCl$_{(sat.)}$ due to the local damage or removal of the passivation layer on the film surface by

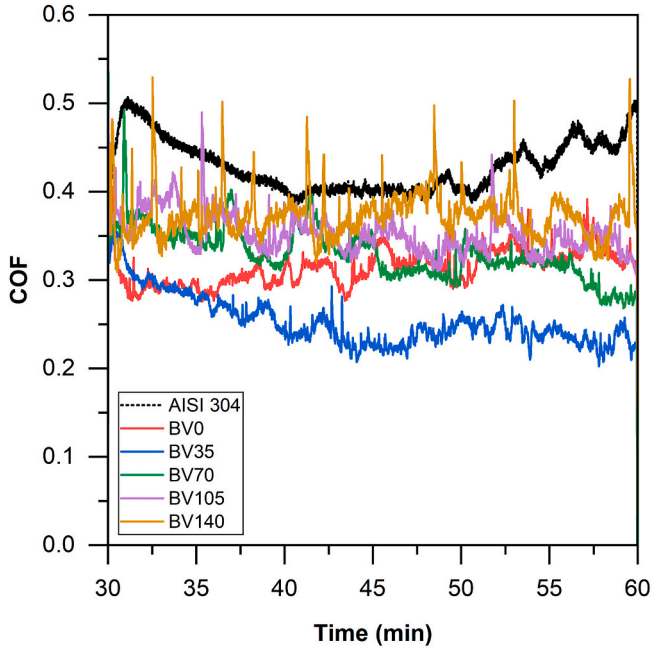

Fig. 10. Friction curves of $Al_xCoCrFeNi$ HEA thin films and AISI 304 stainless steel tested against an Al_2O_3 counterpart in a 3.5 wt.% NaCl aqueous solution.

Table 5
Coefficients of friction and specific wear rates of $Al_xCoCrFeNi$ HEA thin films and AISI 304 stainless steel.

Sample	Coefficient of friction	Specific wear rate ($\times 10^{-6}$ mm^3/(N·m))
AISI 304	0.41 ± 0.08	108 ± 1
BV0	0.31 ± 0.03	71 ± 3
BV35	0.28 ± 0.04	50 ± 8
BV70	0.32 ± 0.04	52 ± 1
BV105	0.35 ± 0.04	58 ± 1
BV140	0.36 ± 0.04	80 ± 9

friction. As a result, a potential difference is established between the depassivated areas (anodic) and the still passive ones (cathodic), thus forming a galvanic coupling that accelerates corrosion on the worn surface. After sliding, the OCPs gradually recover to more positive values, indicating the re-establishment of the passive layer within the wear track [74]. A comparable behavior was observed in CoCrFeNi-based alloys by Wang et al. [75].

The friction curves recorded during the sliding process are illustrated in Fig. 10, and the corresponding average values of coefficient of friction (COF), measured at the steady state during the tribocorrosion tests, are reported in Table 5. The results indicate that the films consistently produced a lower COF compared to the SS substrate. Moreover, as the bias voltage increases (in absolute value) from 0 to −35 V, the average COF value exhibits a slight decrease, followed by a gradual increase with further increases in bias voltage. In particular, the film deposited at −140 V produced the highest COF of 0.36 ± 0.04. The friction curves also become increasingly unstable at higher bias voltages (Fig. 10).

Fig. 11 shows the three-dimensional reconstructions of the wear tracks of the films. Initially, as the bias voltage increases (in absolute value) from 0 to −35 V, the depth and width of the wear tracks decrease. However, with a further increase in bias voltage, there is a subsequent increase, implying a gradual increase in wear volume. Nevertheless, the wear depth consistently remains below the film thickness, suggesting the absence of wear-out failure. Accordingly, the specific wear rate initially decreases and then increases with increasing bias voltage, reaching its minimum value of approximately 50 × 10^{-6} mm^3/(N·m) at −35/−70 V (Table 5). Overall, the wear rate of the films is lower than that of

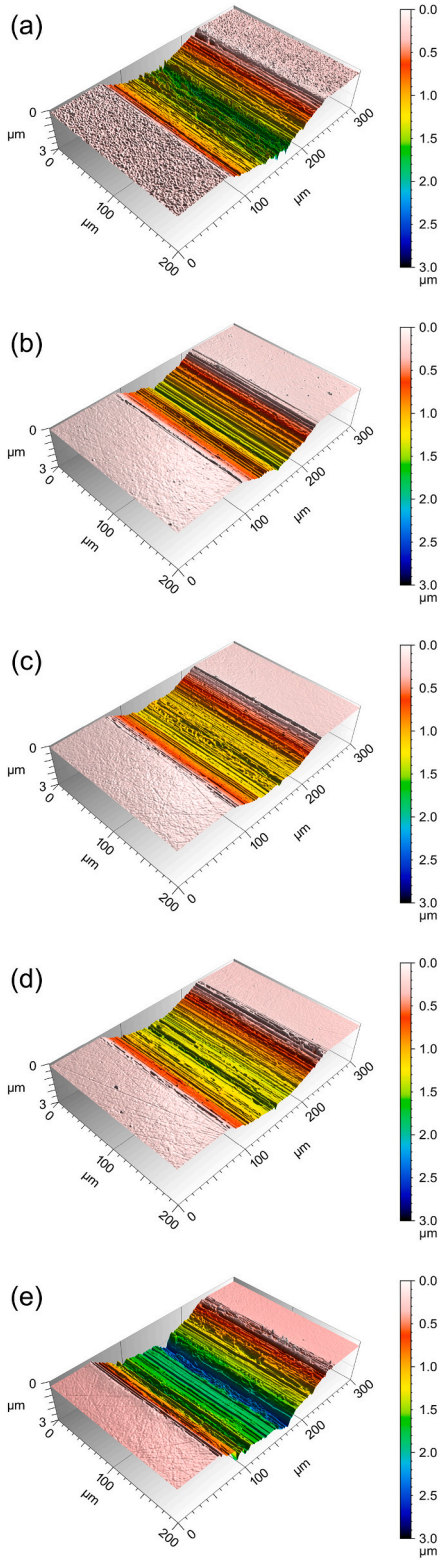

Fig. 11. Three-dimensional wear morphologies of the (a) BV0, (b) BV35, (c) BV70, (d) BV105, and (e) BV140 films.

stainless steel, indicating their effectiveness in improving the wear performance of the substrate. Additionally, optimizing the bias voltage can further enhance the tribocorrosion behavior of these films.

The worn surfaces of the films were observed by SEM to investigate the wear mechanisms. For the unbiased film (Fig. 12(a, b)), the SEM micrographs reveal deep grooves aligned parallel to the sliding

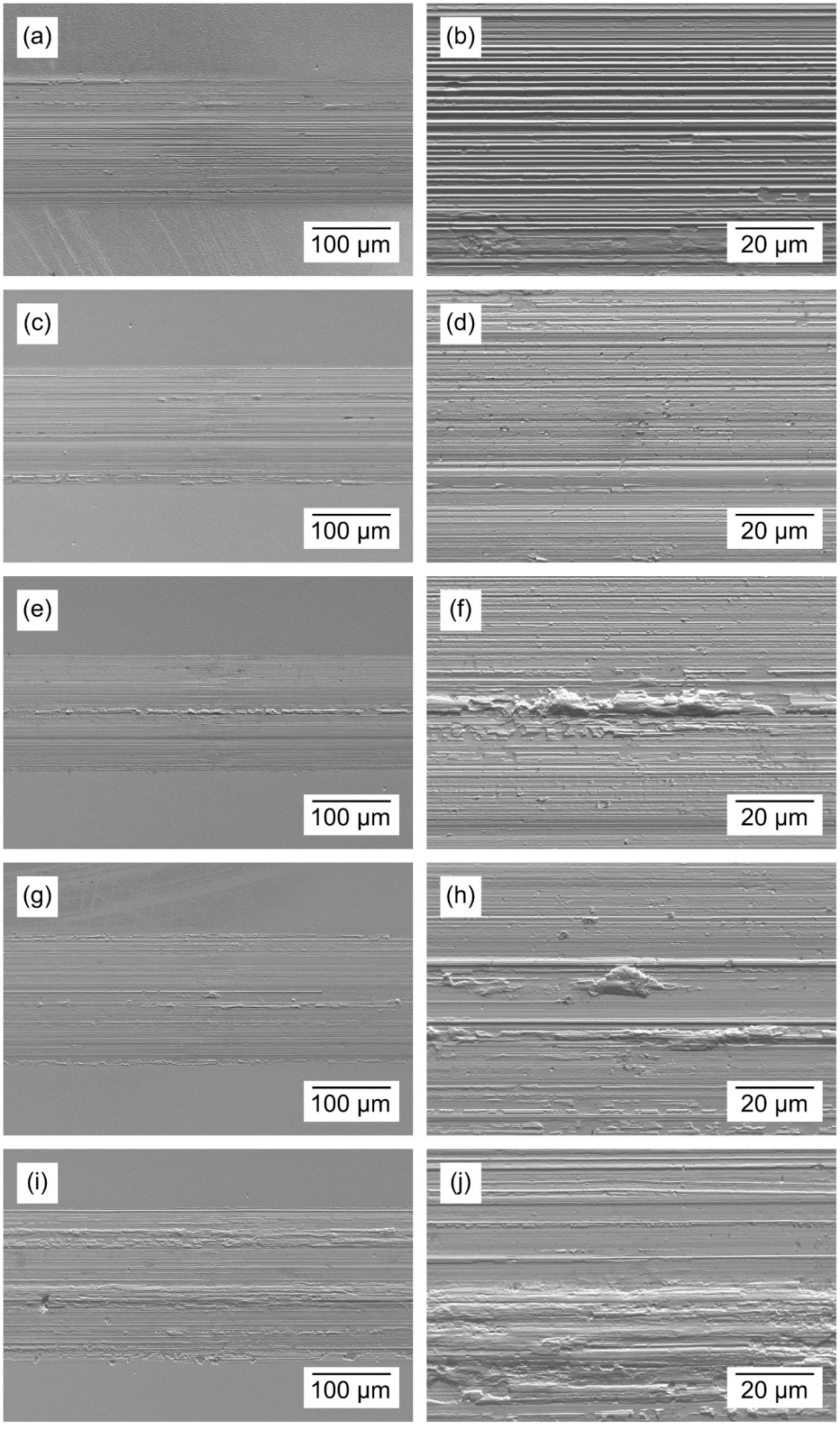

Fig. 12. SEM micrographs showing the worn surfaces of the (a, b) BV0, (c, d) BV35, (e, f) BV70, (g, h) BV105, and (i, j) BV140 films after tribocorrosion testing.

direction, indicating that abrasion is the predominant wear mechanism. As the bias voltage increases (in absolute value) from 0 to −35 V (Fig. 12 (c, d)), the grooves become narrower and shallower, suggesting improved wear resistance. A minor abrasive contribution to friction could also explain the decrease in the measured COF value (Table 5). However, at higher bias voltages (Fig. 12(e-j)), the wear tracks exhibit signs of plastic deformation, characteristic of adhesive wear. This observation is in line with the three-dimensional reconstructions in Fig. 11, where grooves become blurred at higher bias voltage values due to the superposition of plastic deformation effects. The repeated formation and breaking of strong adhesive junctions with the counterpart material would explain the instabilities and spikes observed in the

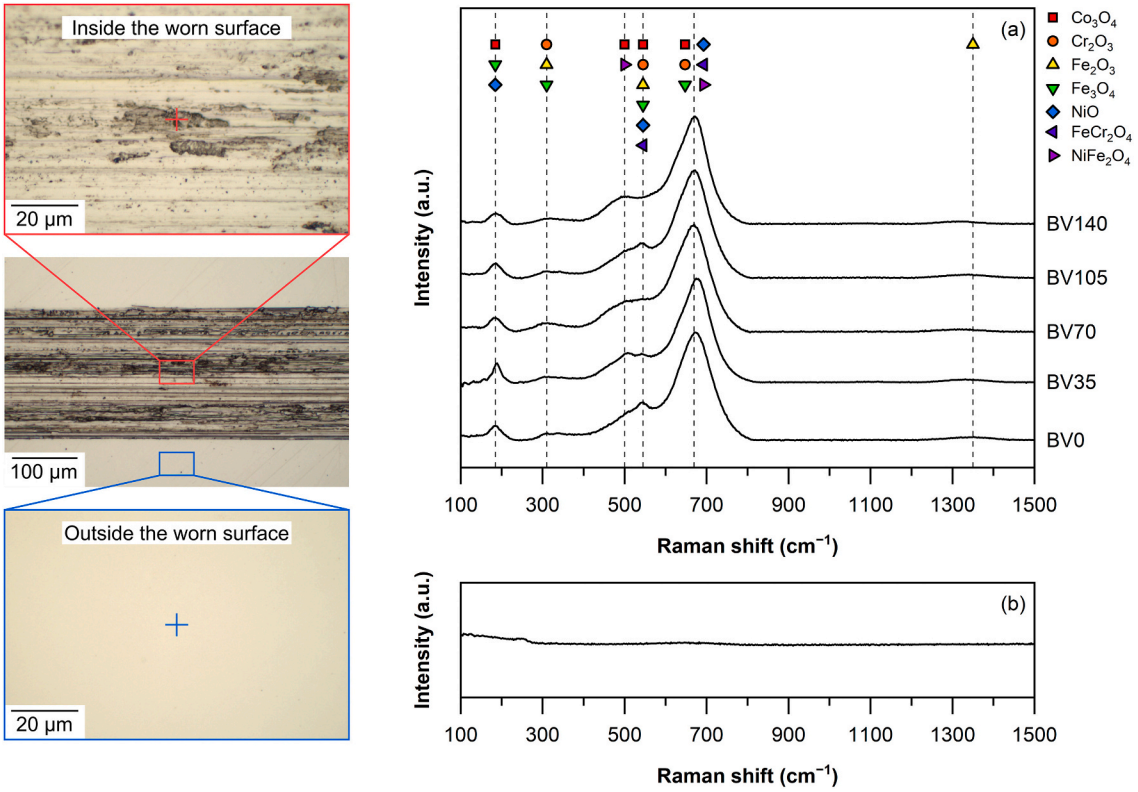

Fig. 13. Raman spectra acquired (a) inside and (b) outside the wear tracks of $Al_xCoCrFeNi$ HEA thin films after tribocorrosion testing, along with the optical micrographs of a representative wear track.

friction curves of the films deposited at higher bias voltages (Fig. 10). Therefore, it can be inferred that the wear mechanism shifts from severe abrasive wear at 0 V to mild abrasive wear at −35 V and eventually to a combination of both abrasive and adhesive wear at higher bias voltages. This change, which could not have been predicted due to the lack of variation in hardness with bias voltage (Table 3), can be partially attributed to the FCC + BCC → FCC phase transformation with increasing bias voltage, as evidenced by the XRD and SAED results in Section 3.3. As previously mentioned, a BCC structure has fewer active slip systems compared to an FCC structure [33], making the material more susceptible to wear-induced cracking and failure. Consequently, the absence of the BCC phase at higher bias voltages, in favor of the FCC phase, likely increases the material's ability to deform plastically under wear conditions, prompting the observed transition in the wear mechanism from purely abrasive wear to a combination of abrasive and adhesive wear. The increasingly ductile response of the films observed during scratch testing (Section 3.5) further supports the increased tendency toward adhesive wear. However, isolating the specific impact of this phase transformation on wear resistance is challenging, as higher bias voltages also induce other concurrent effects, such as microstructural refinement and variation in residual stress state, all of which can influence the wear behavior. Therefore, while the transition to an FCC structure may improve ductility, which aligns with the observed shift in the wear mechanism, discerning its contribution to wear resistance from other co-evolving film characteristics requires further investigation.

The phase composition of the debris found in the wear tracks after tribocorrosion testing was examined by micro-Raman spectroscopy. As displayed in Fig. 13(b), no Raman signal is detected outside the worn surface, indicating its metallic nature with no significant oxidation other than a very thin passive layer undetectable by visible-light techniques. In contrast, distinct Raman peaks are evident within the wear track (Fig. 13(a)), attributed to spinel oxides of the alloying elements [76]. However, distinguishing between these oxides is impractical because of their similar peak positions. These structures allow for extensive cation substitution, resulting in the formation of continuous solid solutions. Consequently, the worn surface likely consists of solid solution spinel oxides containing a mix of cations resulting from tribologically induced oxidation reactions, wherein fine debris particles transform into oxides containing a homogeneous distribution of metallic elements.

4. Conclusions

In this work, $Al_xCoCrFeNi$ HEA thin films were deposited by HiPIMS to investigate the effect of varying the substrate bias voltage from 0 to −140 V on their structure and properties. The key findings can be summarized as follows:

- When the bias voltage exceeded −70 V, the Al content decreased from 10 to 5 at.%, accompanied by a transition from a dual-phase FCC + BCC structure to a single-phase FCC structure. The columnar microstructure also became increasingly dense and fine, to the extent that columnar grains were detectable only by TEM.
- The residual stress state within the films shifted from tensile to compressive due to the more energetic film growth conditions at higher bias voltages. Nevertheless, the hardness of the films remained constant at approximately 9 GPa, showing no significant variations with increasing bias voltage. The scratch response of the films transitioned from brittle cracking when no bias voltage was applied to ductile deformation upon bias voltage application, accompanied by the formation of wrinkle-like ripples along the edges of the scratch tracks.
- The potentiodynamic polarization curves revealed a significant improvement in the electrochemical performance of the films deposited at higher bias voltages, ascribable to their dense and fine-grained microstructure, which effectively hinders the diffusion of corrosive agents.

- The films deposited at intermediate bias voltages exhibited superior tribocorrosion performance, with wear rates around 50 × 10^{-6} mm^3/(N·m). However, further increasing the bias voltage led to increased material loss, attributable to a change in the wear mechanism from purely abrasive to a combination of abrasive and adhesive effects.
- Overall, all films demonstrated superior wear and corrosion resistance in simulated seawater compared to the AISI 304 stainless steel substrate, affirming their promising potential as protective films in marine engineering and related industries. Moreover, by adjusting the substrate bias voltage, their performance can be further optimized to address specific needs, depending on whether pure corrosion or tribocorrosion resistance is required.

CRediT authorship contribution statement

Alessandro Togni: Writing – review & editing, Writing – original draft, Visualization, Methodology, Investigation, Formal analysis. **Francesco Montagner:** Writing – review & editing, Methodology, Investigation. **Enrico Miorin:** Writing – review & editing, Conceptualization. **Cecilia Mortalò:** Writing – review & editing. **Valentina Zin:** Writing – review & editing, Methodology, Investigation, Formal analysis. **Giovanni Bolelli:** Writing – review & editing, Validation. **Luca Lusvarghi:** Supervision. **Stefano Frabboni:** Investigation. **Gian Carlo Gazzadi:** Investigation. **Lidia Armelao:** Funding acquisition. **Silvia Maria Deambrosis:** Writing – review & editing, Supervision, Project administration, Methodology, Investigation, Conceptualization.

Declaration of competing interest

The authors declare that they have no known competing financial interests or personal relationships that could have appeared to influence the work reported in this paper.

Acknowledgements

This work was partially funded as part of the research programme “Ricerca di Sistema Elettrico Nazionale” (RdS 2019-2021), thanks to an agreement between the Italian Ministry of Economic Development and the National Research Council of Italy.

Data availability

Data will be made available on request.

References

[1] J.-W. Yeh, S.-K. Chen, S.-J. Lin, J.-Y. Gan, T.-S. Chin, T.-T. Shun, C.-H. Tsau, S.-Y. Chang, Nanostructured high-entropy alloys with multiple principal elements: novel alloy design concepts and outcomes, Adv. Eng. Mater. 6 (2004) 299–303, https://doi.org/10.1002/adem.200300567.
[2] C.-J. Tong, M.-R. Chen, J.-W. Yeh, S.-J. Lin, S.-K. Chen, T.-T. Shun, S.-Y. Chang, Mechanical performance of the AlxCoCrCuFeNi high-entropy alloy system with multiprincipal elements, Metall. Mater. Trans. A 36 (2005) 1263–1271, https://doi.org/10.1007/s11661-005-0218-9.
[3] B. Schuh, F. Mendez-Martin, B. Völker, E.P. George, H. Clemens, R. Pippan, A. Hohenwarter, Mechanical properties, microstructure and thermal stability of a nanocrystalline CoCrFeMnNi high-entropy alloy after severe plastic deformation, Acta Mater. 96 (2015) 258–268, https://doi.org/10.1016/j.actamat.2015.06.025.
[4] M.-H. Chuang, M.-H. Tsai, W.-R. Wang, S.-J. Lin, J.-W. Yeh, Microstructure and wear behavior of AlxCo1.5CrFeNi1.5Tiy high-entropy alloys, Acta Mater. 59 (2011) 6308–6317, https://doi.org/10.1016/j.actamat.2011.06.041.
[5] Y.Y. Chen, T. Duval, U.D. Hung, J.W. Yeh, H.C. Shih, Microstructure and electrochemical properties of high entropy alloys—a comparison with type-304 stainless steel, Corros. Sci. 47 (2005) 2257–2279, https://doi.org/10.1016/j.corsci.2004.11.008.
[6] W. Li, P. Liu, P.K. Liaw, Microstructures and properties of high-entropy alloy films and coatings: a review, Mater. Res. Lett. 6 (2018) 199–229, https://doi.org/10.1080/21663831.2018.1434248.
[7] T.K. Chen, T.T. Shun, J.W. Yeh, M.S. Wong, Nanostructured nitride films of multi-element high-entropy alloys by reactive DC sputtering, Surf. Coat. Technol. 188–189 (2004) 193–200, https://doi.org/10.1016/j.surfcoat.2004.08.023.
[8] C.-H. Lai, S.-J. Lin, J.-W. Yeh, S.-Y. Chang, Preparation and characterization of AlCrTaTiZr multi-element nitride coatings, Surf. Coat. Technol. 201 (2006) 3275–3280, https://doi.org/10.1016/j.surfcoat.2006.06.048.
[9] H.-W. Chang, P.-K. Huang, J.-W. Yeh, A. Davison, C.-H. Tsau, C.-C. Yang, Influence of substrate bias, deposition temperature and post-deposition annealing on the structure and properties of multi-principal-component (AlCrMoSiTi)N coatings, Surf. Coat. Technol. 202 (2008) 3360–3366, https://doi.org/10.1016/j.surfcoat.2007.12.014.
[10] P.-K. Huang, J.-W. Yeh, T.-T. Shun, S.-K. Chen, Multi-principal-element alloys with improved oxidation and wear resistance for thermal spray coating, Adv. Eng. Mater. 6 (2004) 74–78, https://doi.org/10.1002/adem.200300507.
[11] L.M. Wang, C.C. Chen, J.W. Yeh, S.T. Ke, The microstructure and strengthening mechanism of thermal spray coating NixCo0.6Fe0.2CrySizAlTi0.2 high-entropy alloys, Mater. Chem. Phys. 126 (2011) 880–885, https://doi.org/10.1016/j.matchemphys.2010.12.022.
[12] A.S.M. Ang, C.C. Berndt, M.L. Sesso, A. Anupam, P. S, R.S. Kottada, B.S. Murty, Plasma-sprayed high entropy alloys: microstructure and properties of AlCoCrFeNi and MnCoCrFeNi, Metallurgical and Materials Transactions A 46 (2015) 791–800, https://doi.org/10.1007/s11661-014-2644-z.
[13] C.-Z. Yao, P. Zhang, M. Liu, G.-R. Li, J.-Q. Ye, P. Liu, Y.-X. Tong, Electrochemical preparation and magnetic study of Bi–Fe–Co–Ni–Mn high entropy alloy, Electrochim. Acta 53 (2008) 8359–8365, https://doi.org/10.1016/j.electacta.2008.06.036.
[14] V. Soare, M. Burada, I. Constantin, D. Mitrică, V. Bădiliţă, A. Caragea, M. Tărcolea, Electrochemical deposition and microstructural characterization of AlCrFeMnNi and AlCrCuFeMnNi high entropy alloy thin films, Appl. Surf. Sci. 358 (2015) 533–539, https://doi.org/10.1016/j.apsusc.2015.07.142.
[15] H. Zhang, Y. Pan, Y.-Z. He, Synthesis and characterization of FeCoNiCrCu high-entropy alloy coating by laser cladding, Mater Des 32 (2011) 1910–1915, https://doi.org/10.1016/j.matdes.2010.12.001.
[16] C. Huang, Y. Zhang, R. Vilar, J. Shen, Dry sliding wear behavior of laser clad TiVCrAlSi high entropy alloy coatings on Ti–6Al–4V substrate, Mater. Des. 41 (2012) 338–343, https://doi.org/10.1016/j.matdes.2012.04.049.
[17] J.W. Bradley, S. Thompson, Y.A. Gonzalvo, Measurement of the plasma potential in a magnetron discharge and the prediction of the electron drift speeds, Plasma Sources Sci. Technol. 10 (2001) 490–501, https://doi.org/10.1088/0963-0252/10/3/314.
[18] I. Petrov, A. Myers, J.E. Greene, J.R. Abelson, Mass and energy resolved detection of ions and neutral sputtered species incident at the substrate during reactive magnetron sputtering of Ti in mixed Ar+N2 mixtures, J. Vac. Sci. Technol. A 12 (1994) 2846–2854, https://doi.org/10.1116/1.578955.
[19] C. Christou, Z.H. Barber, Ionization of sputtered material in a planar magnetron discharge, J. Vac. Sci. Technol. A 18 (2000) 2897–2907, https://doi.org/10.1116/1.1312370.
[20] V. Kouznetsov, K. Macák, J.M. Schneider, U. Helmersson, I. Petrov, A novel pulsed magnetron sputter technique utilizing very high target power densities, Surf. Coat. Technol. 122 (1999) 290–293, https://doi.org/10.1016/S0257-8972(99)00292-3.
[21] U. Helmersson, M. Lattemann, J. Bohlmark, A.P. Ehiasarian, J.T. Gudmundsson, Ionized physical vapor deposition (IPVD): a review of technology and applications, Thin Solid Films 513 (2006) 1–24, https://doi.org/10.1016/j.tsf.2006.03.033.
[22] K. Sarakinos, J. Alami, S. Konstantinidis, High power pulsed magnetron sputtering: a review on scientific and engineering state of the art, Surf. Coat. Technol. 204 (2010) 1661–1684, https://doi.org/10.1016/j.surfcoat.2009.11.013.
[23] J. Bohlmark, J.T. Gudmundsson, J. Alami, M. Latteman, U. Helmersson, Spatial electron density distribution in a high-power pulsed magnetron discharge, IEEE Trans. Plasma Sci. 33 (2005) 346–347, https://doi.org/10.1109/TPS.2005.845022.
[24] J. Alami, J.T. Gudmundsson, J. Bohlmark, J. Birch, U. Helmersson, Plasma dynamics in a highly ionized pulsed magnetron discharge, Plasma Sources Sci. Technol. 14 (2005) 525–531, https://doi.org/10.1088/0963-0252/14/3/015.
[25] J. Bohlmark, J. Alami, C. Christou, A.P. Ehiasarian, U. Helmersson, Ionization of sputtered metals in high power pulsed magnetron sputtering, J. Vac. Sci. Technol. A 23 (2005) 18–22, https://doi.org/10.1116/1.1818135.
[26] J. Alami, P.O.Å. Persson, D. Music, J.T. Gudmundsson, J. Bohlmark, U. Helmersson, Ion-assisted physical vapor deposition for enhanced film properties on nonflat surfaces, J. Vac. Sci. Technol. A 23 (2005) 278–280, https://doi.org/10.1116/1.1861049.
[27] M. Samuelsson, D. Lundin, J. Jensen, M.A. Raadu, J.T. Gudmundsson, U. Helmersson, On the film density using high power impulse magnetron sputtering, Surf. Coat. Technol. 205 (2010) 591–596, https://doi.org/10.1016/j.surfcoat.2010.07.041.
[28] Y. Xu, G. Li, G. Li, F. Gao, Y. Xia, Effect of bias voltage on the growth of super-hard (AlCrTiVZr)N high-entropy alloy nitride films synthesized by high power impulse magnetron sputtering, Appl. Surf. Sci. 564 (2021) 150417, https://doi.org/10.1016/j.apsusc.2021.150417.
[29] X.K. Zeng, Y.T. Li, X.D. Zhang, M. Liu, J.Z. Ye, X.L. Qiu, X. Jiang, Y.X. Leng, Effect of bias voltage on the structure and properties of CuNiTiNbCr dual-phase high entropy alloy films, J. Alloys Compd. 931 (2023) 167371, https://doi.org/10.1016/j.jallcom.2022.167371.
[30] Y.-F. Kao, T.-J. Chen, S.-K. Chen, J.-W. Yeh, Microstructure and mechanical property of as-cast, −homogenized, and -deformed AlxCoCrFeNi (0≤x≤2) high-entropy alloys, J. Alloys Compd. 488 (2009) 57–64, https://doi.org/10.1016/j.jallcom.2009.08.090.
[31] W.-R. Wang, W.-L. Wang, S.-C. Wang, Y.-C. Tsai, C.-H. Lai, J.-W. Yeh, Effects of Al addition on the microstructure and mechanical property of AlxCoCrFeNi high-

entropy alloys, Intermetallics (Barking) 26 (2012) 44–51, https://doi.org/10.1016/j.intermet.2012.03.005.
[32] Y. Shi, B. Yang, X. Xie, J. Brechtl, K.A. Dahmen, P.K. Liaw, Corrosion of AlxCoCrFeNi high-entropy alloys: Al-content and potential scan-rate dependent pitting behavior, Corros. Sci. 119 (2017) 33–45, https://doi.org/10.1016/j.corsci.2017.02.019.
[33] Y. Zhang, T.T. Zuo, Z. Tang, M.C. Gao, K.A. Dahmen, P.K. Liaw, Z.P. Lu, Microstructures and properties of high-entropy alloys, Prog. Mater. Sci. 61 (2014) 1–93, https://doi.org/10.1016/j.pmatsci.2013.10.001.
[34] V. Zin, F. Montagner, E. Miorin, C. Mortalò, R. Tinazzi, G. Bolelli, L. Lusvarghi, A. Togni, S. Frabboni, G. Gazzadi, A. Mescola, G. Paolicelli, L. Armelao, S. M. Deambrosis, Effect of Mo content on the microstructure and mechanical properties of CoCrFeNiMox HEA coatings deposited by high power impulse magnetron sputtering, Surf. Coat. Technol. 476 (2024) 130244, https://doi.org/10.1016/j.surfcoat.2023.130244.
[35] G. Greczynski, J. Lu, J. Jensen, I. Petrov, J.E. Greene, S. Bolz, W. Kölker, C. Schiffers, O. Lemmer, L. Hultman, Metal versus rare-gas ion irradiation during Ti1−xAlxN film growth by hybrid high power pulsed magnetron/dc magnetron co-sputtering using synchronized pulsed substrate bias, J. Vac. Sci. Technol. A 30 (2012), https://doi.org/10.1116/1.4750485.
[36] G.G. Stoney, The tension of metallic films deposited by electrolysis, Proceedings of the Royal Society of London. Series A, Containing Papers of a Mathematical and Physical Character 82 (1909) 172–175, https://doi.org/10.1098/rspa.1909.0021.
[37] W.D. Nix, Mechanical properties of thin films, Metall. Trans. A. 20 (1989) 2217–2245, https://doi.org/10.1007/BF02666659.
[38] A.M. Korsunsky, M.R. McGurk, S.J. Bull, T.F. Page, On the hardness of coated systems, Surf. Coat. Technol. 99 (1998) 171–183, https://doi.org/10.1016/S0257-8972(97)00522-7.
[39] W.C. Oliver, G.M. Pharr, An improved technique for determining hardness and elastic modulus using load and displacement sensing indentation experiments, J. Mater. Res. 7 (1992) 1564–1583, https://doi.org/10.1557/JMR.1992.1564.
[40] W.C. Oliver, G.M. Pharr, Measurement of hardness and elastic modulus by instrumented indentation: advances in understanding and refinements to methodology, J. Mater. Res. 19 (2004) 3–20, https://doi.org/10.1557/jmr.2004.19.1.3.
[41] S. Zhang, D. Sun, Y. Fu, H. Du, Q. Zhang, Effect of sputtering target power density on topography and residual stress during growth of nanocomposite nc-TiN/a-SiNx thin films, Diamond Relat. Mater. 13 (2004) 1777–1784, https://doi.org/10.1016/j.diamond.2004.03.008.
[42] I. Petrov, L. Hultman, U. Helmersson, J.-E. Sundgren, J.E. Greene, Microstructure modification of TiN by ion bombardment during reactive sputter deposition, Thin Solid Films 169 (1989) 299–314, https://doi.org/10.1016/0040-6090(89)90713-X.
[43] D.M. Mattox, Particle bombardment effects on thin-film deposition: a review, J. Vac. Sci. Technol. A 7 (1989) 1105–1114, https://doi.org/10.1116/1.576238.
[44] N. Laegreid, G.K. Wehner, Sputtering yields of metals for Ar+ and ne+ ions with energies from 50 to 600 ev, J. Appl. Phys. 32 (1961) 365–369, https://doi.org/10.1063/1.1736012.
[45] X. Zhang, V. Pelenovich, X. Zeng, Q. Wan, J. Liu, A. Pogrebnjak, Y. Guo, Y. Liu, Y. Lei, B. Yang, Unravel hardening mechanism of AlCrNbSiTi high-entropy alloy coatings, J. Alloys Compd. 965 (2023) 171222, https://doi.org/10.1016/j.jallcom.2023.171222.
[46] J. Wang, S. Kuang, X. Yu, L. Wang, W. Huang, Tribo-mechanical properties of CrNbTiMoZr high-entropy alloy film synthesized by direct current magnetron sputtering, Surf. Coat. Technol. 403 (2020) 126374, https://doi.org/10.1016/j.surfcoat.2020.126374.
[47] X. Yu, J. Wang, L. Wang, W. Huang, Fabrication and characterization of CrNbSiTiZr high-entropy alloy films by radio-frequency magnetron sputtering via tuning substrate bias, Surf. Coat. Technol. 412 (2021) 127074, https://doi.org/10.1016/j.surfcoat.2021.127074.
[48] P.-K. Huang, J.-W. Yeh, Effects of substrate bias on structure and mechanical properties of (AlCrNbSiTiV)N coatings, J. Phys. D Appl. Phys. 42 (2009) 115401, https://doi.org/10.1088/0022-3727/42/11/115401.
[49] W.-J. Shen, M.-H. Tsai, Y.-S. Chang, J.-W. Yeh, Effects of substrate bias on the structure and mechanical properties of (Al1.5CrNb0.5Si0.5Ti)Nx coatings, Thin Solid Films 520 (2012) 6183–6188, https://doi.org/10.1016/j.tsf.2012.06.002.
[50] M.-H. Hsieh, M.-H. Tsai, W.-J. Shen, J.-W. Yeh, Structure and properties of two Al–Cr–Nb–Si–Ti high-entropy nitride coatings, Surf. Coat. Technol. 221 (2013) 118–123, https://doi.org/10.1016/j.surfcoat.2013.01.036.
[51] W.-L. Lo, S.-Y. Hsu, Y.-C. Lin, S.-Y. Tsai, Y.-T. Lai, J.-G. Duh, Improvement of high entropy alloy nitride coatings (AlCrNbSiTiMo)N on mechanical and high temperature tribological properties by tuning substrate bias, Surf. Coat. Technol. 401 (2020) 126247, https://doi.org/10.1016/j.surfcoat.2020.126247.
[52] X. Zhang, V. Pelenovich, Y. Liu, X. Ke, J. Zhang, B. Yang, G. Ma, M. Li, X. Wang, Effect of bias voltages on microstructure and properties of (TiVCrNbSiTaBY)N high entropy alloy nitride coatings deposited by RF magnetron sputtering, Vacuum 195 (2022) 110710, https://doi.org/10.1016/j.vacuum.2021.110710.
[53] A. Anders, A structure zone diagram including plasma-based deposition and ion etching, Thin Solid Films 518 (2010) 4087–4090, https://doi.org/10.1016/j.tsf.2009.10.145.
[54] X.B. Feng, W. Fu, J.Y. Zhang, J.T. Zhao, J. Li, K. Wu, G. Liu, J. Sun, Effects of nanotwins on the mechanical properties of AlxCoCrFeNi high entropy alloy thin films, Scr. Mater. 139 (2017) 71–76, https://doi.org/10.1016/j.scriptamat.2017.06.009.
[55] S. Guo, C. Ng, J. Lu, C.T. Liu, Effect of valence electron concentration on stability of fcc or bcc phase in high entropy alloys, J. Appl. Phys. 109 (2011), https://doi.org/10.1063/1.3587228.
[56] S. Guo, C.T. Liu, Phase stability in high entropy alloys: formation of solid-solution phase or amorphous phase, Prog. Nat. Sci.: Mater. Int. 21 (2011) 433–446, https://doi.org/10.1016/S1002-0071(12)60080-X.
[57] A.J. Zaddach, C. Niu, C.C. Koch, D.L. Irving, Mechanical properties and stacking fault energies of NiFeCrCoMn high-entropy alloy, JOM 65 (2013) 1780–1789, https://doi.org/10.1007/s11837-013-0771-4.
[58] J.-J. Wang, F.-Y. Ouyang, Nanotwinned medium entropy alloy CoCrFeNi thin films with ultra-high hardness: modifying residual stress without scarifying hardness through tuning substrate bias, Surf. Coat. Technol. 434 (2022) 128191, https://doi.org/10.1016/j.surfcoat.2022.128191.
[59] H. Oettel, R. Wiedemann, Residual stresses in PVD hard coatings, Surf. Coat. Technol. 76–77 (1995) 265–273, https://doi.org/10.1016/0257-8972(95)02581-2.
[60] C.A. Davis, A simple model for the formation of compressive stress in thin films by ion bombardment, Thin Solid Films 226 (1993) 30–34, https://doi.org/10.1016/0040-6090(93)90201-Y.
[61] J.A. Thornton, D.W. Hoffman, Stress-related effects in thin films, Thin Solid Films 171 (1989) 5–31, https://doi.org/10.1016/0040-6090(89)90030-8.
[62] S.J. Bull, A.M. Jones, A.R. McCabe, Residual stress in ion-assisted coatings, Surf. Coat. Technol. 54–55 (1992) 173–179, https://doi.org/10.1016/S0257-8972(09)90046-9.
[63] Y. Xu, G. Li, Y. Xia, Synthesis and characterization of super-hard AlCrTiVZr high-entropy alloy nitride films deposited by HiPIMS, Appl. Surf. Sci. 523 (2020) 146529, https://doi.org/10.1016/j.apsusc.2020.146529.
[64] S. Kuang, J. Wang, L. Wang, W. Huang, Z. Zhou, Improvement of the mechanical and the tribological properties of CrNbTiMoZr coatings through the incorporation of carbon and the adjustment of the substrate bias voltage, Surf. Coat. Technol. 412 (2021) 127064, https://doi.org/10.1016/j.surfcoat.2021.127064.
[65] R.F. Bunshah, Handbook of Hard Coatings: Deposition Technologies, Properties and Applications, Elsevier, 2002.
[66] C. Li, J.C. Li, M. Zhao, Q. Jiang, Effect of aluminum contents on microstructure and properties of AlxCoCrFeNi alloys, J. Alloys Compd. 504 (2010) S515–S518, https://doi.org/10.1016/j.jallcom.2010.03.111.
[67] P.J. Burnett, D.S. Rickerby, The relationship between hardness and scratch adhesion, Thin Solid Films 154 (1987) 403–416, https://doi.org/10.1016/0040-6090(87)90382-8.
[68] S.J. Bull, Failure modes in scratch adhesion testing, Surf. Coat. Technol. 50 (1991) 25–32, https://doi.org/10.1016/0257-8972(91)90188-3.
[69] S. Zhang, C.L. Wu, C.H. Zhang, M. Guan, J.Z. Tan, Laser surface alloying of FeCoCrAlNi high-entropy alloy on 304 stainless steel to enhance corrosion and cavitation erosion resistance, Opt. Laser Technol. 84 (2016) 23–31, https://doi.org/10.1016/j.optlastec.2016.04.011.
[70] N.G. Kipkirui, T.-T. Lin, R.S. Kiplangat, J.-W. Lee, S.-H. Chen, HiPIMS and RF magnetron sputtered Al0.5CoCrFeNi2Ti0.5 HEA thin-film coatings: synthesis and characterization, Surf. Coat. Technol. 449 (2022) 128988, https://doi.org/10.1016/j.surfcoat.2022.128988.
[71] Z. An, H. Jia, Y. Wu, P.D. Rack, A.D. Patchen, Y. Liu, Y. Ren, N. Li, P.K. Liaw, Solid-solution CrCoCuFeNi high-entropy alloy thin films synthesized by sputter deposition, Mater. Res. Lett. 3 (2015) 203–209, https://doi.org/10.1080/21663831.2015.1048904.
[72] Y. Shi, B. Yang, P.D. Rack, S. Guo, P.K. Liaw, Y. Zhao, High-throughput synthesis and corrosion behavior of sputter-deposited nanocrystalline Alx(CoCrFeNi)100-x combinatorial high-entropy alloys, Mater. Des. 195 (2020) 109018, https://doi.org/10.1016/j.matdes.2020.109018.
[73] Q.H. Li, T.M. Yue, Z.N. Guo, X. Lin, Microstructure and corrosion properties of AlCoCrFeNi high entropy alloy coatings deposited on AISI 1045 steel by the electrospark process, Metallurgical and Materials Transactions A 44 (2013) 1767–1778, https://doi.org/10.1007/s11661-012-1535-4.
[74] P. Ponthiaux, F. Wenger, D. Drees, J.P. Celis, Electrochemical techniques for studying tribocorrosion processes, Wear 256 (2004) 459–468, https://doi.org/10.1016/S0043-1648(03)00556-8.
[75] J. Wang, W. Wen, J. Cheng, L. Dai, S. Li, X. Zhang, Y. Yang, H. Li, X. Hou, B. Wu, J. Wu, Tribocorrosion behavior of high-entropy alloys FeCrNiCoM (M = Al, Mo) in artificial seawater, Corros. Sci. 218 (2023) 111165, https://doi.org/10.1016/j.corsci.2023.111165.
[76] J. Dąbrowa, M. Stygar, A. Mikuła, A. Knapik, K. Mroczka, W. Tejchman, M. Danielewski, M. Martin, Synthesis and microstructure of the (Co,Cr,Fe,Mn,Ni)3O4 high entropy oxide characterized by spinel structure, Mater. Lett. 216 (2018) 32–36, https://doi.org/10.1016/j.matlet.2017.12.148.